atmosphere

MDPI

Article

Influences of MJO on the Diurnal Variation and Associated Offshore Propagation of Rainfall near Western Coast of Sumatra

Bojun Zhu [1], Yu Du [2,3,4,*] and Zhiqiu Gao [1,5]

[1] Climate and Weather Disasters Collaborative Innovation Center, School of Applied Meteorology, Nanjing University of Information Science & Technology, Nanjing 210044, China; bojun.zhu@nuist.edu.cn (B.Z.); zgao@mail.iap.ac.cn (Z.G.)
[2] School of Atmospheric Sciences, and Guangdong Province Key Laboratory for Climate Change and Natural Disaster Studies, Sun Yat-sen University, Zhuhai 519082, China
[3] Southern Marine Science and Engineering Guangdong Laboratory (Zhuhai), Zhuhai 519082, China
[4] Key Laboratory of Tropical Atmosphere-Ocean System (Sun Yat-sen University), Ministry of Education, Zhuhai 519082, China
[5] State Key Laboratory of Atmospheric Boundary Layer Physics and Atmospheric Chemistry, Institute of Atmospheric Physics, Chinese Academy of Sciences, Beijing 100029, China
* Correspondence: duyu7@mail.sysu.edu.cn

Abstract: Madden-Julian Oscillation (MJO) plays an important role in modulating precipitation at Maritime Continent (MC) not only on a larger scale, but also in the diurnal cycle. Diurnal rainfall offshore propagation is one of the most evident features near coasts. This study investigates the impacts of MJO on diurnal rainfall and its offshore propagation at the western coast of Sumatra during boreal winters using ERA5 reanalysis. The real-time multivariate MJO (RMM) index was applied to locate the active MJO convection through eight different phases, in the western hemisphere and Africa in P8–P1, at the Indian Ocean in P2–P3, at MC in P4–P5, and the western Pacific Ocean in P6–P7. The rainfall characteristics, including the daily rate, the absolute and normalized diurnal variation amplitudes, and the strengths of diurnal offshore propagation, not only depend on active/inactive MJO stages but also vary under different MJO phases, through the combined modulations of large-scale backgrounds and local-scale land–sea circulations. The offshore rainfall propagation is associated with meso-large-scale gravity waves generated from land–sea thermal contrast and thus is affected by the radiation effect of cloud under different MJO phases. The stronger wave signals in P8–P1 and P6–P7 enhance the diurnal rainfall variation amplitudes away from the coast, while the strong coupling of moist convection with gravity waves contributes greatly to the diurnal rainfall cycle in P2–P3.

Keywords: MJO; rainfall; diurnal variation; land–sea circulation; gravity wave

Citation: Zhu, B.; Du, Y.; Gao, Z. Influences of MJO on the Diurnal Variation and Associated Offshore Propagation of Rainfall near Western Coast of Sumatra. *Atmosphere* **2022**, *13*, 330. https://doi.org/10.3390/atmos13020330

Academic Editor: Stefan Liess

Received: 13 January 2022
Accepted: 14 February 2022
Published: 16 February 2022

1. Introduction

Madden–Julian Oscillation (MJO) [1,2] is a dominant intra-seasonal tropical oscillation, characterized by an eastward propagation of about 5 m s^{-1} and a zonal shift of 12,000–20,000 km within 30–100 days [3]. A number of previous studies have documented noticeable influences of MJO on global precipitation by the modulation of background-wind convergence and vapor transportation [4–8]. The most significant oscillations and influences usually occurred during boreal winters [9–13]. Those findings improved our understanding of the formation and development of precipitation controlled by the large-scale forces during an MJO event.

Maritime Continent (MC) is the general designation of tropical seas and islands between Indian Ocean and Pacific Ocean, with a zonal span of around 5000 km [14] and variations in topography, shape and area [15]. As one of the regions with most active convection and great influences by factors such as MJO or convectively coupled equatorial waves (CCEWs), MC generates frequent precipitation all over the years, and the

associated latent heat from rainfall becomes one of the main energy sources driving global circulation [16], which plays nonnegligible roles in global weather and climate [17–20]. The diurnal variation of rainfall is a common phenomenon in coastal regions, including MC; more specifically, it is often characterized by offshore propagation near the coasts, whose mechanisms are closely related to gravity waves [21–24], background-wind modulations [21,23,25], land–sea breezes [26–29], and cold pool outflows [30–32].

Previous studies revealed the MJO's influences on the diurnal variation of coastal rainfall at MC via sea surface temperature (SST), background winds and convection using reanalysis, satellite or radar data [33–37], which are as important as the roles of other factors, for example, different types of CCEWs that modulate sub-seasonal or intra-seasonal convective activities uniquely, across synoptic or longer timescales [38–42]. However, a controversial question has remained regarding which MJO phase undertakes the most significant diurnal precipitation variation, as some studies suggested the arrival of the MJO's active convection at MC [34,35], while others recognized the preconditioning stage narrowly prior to that arrival [43,44]. Additionally, Rauniyar and Walsh [45] concluded that the MJO convective disturbance was favorable for coastal precipitation but unfavorable for landside precipitation. Although these studies on various MJO events might draw distinguished conclusions, very limited analysis has been conducted for detailed explanation. The remarks above reflect the difficulty to regard MC as a broad whole since the impacts of each MJO phase could vary among different MC islands.

The Sumatra Island investigated in this paper lies to the west of Indonesia, as one of the giant islands at MC that exhibits the earliest responses to the MJO as it moves eastward, and has attracted increasing attention for studying the MJO's impacts on diurnal rainfall variations [24,25,29,36,37,46–48] and rainfall extremes [49,50]. The study from Zhu et al. [51] also reveals the difficulty of improving numerical rainfall simulations through local-scale data assimilation in this area under the MJO active phase, due to the large-scale convective envelope as a dominating convection driver. The inconsistency between coastal and surrounding features of diurnal precipitation variation, together with multi-scale synoptic modulations, were exhibited in some studies [39,41], but their variations among different MJO phases still lack enough discussion. In addition, most of the studies focus on how the MJO affects the diurnal variation at Sumatra, but the effects on the diurnal offshore propagation are generally unclear. According to the study from Vincent and Lane [36], the diurnal propagation at western Sumatra is much stronger than that at other MC islands such as Java and New Guinea, as one nonnegligible characteristic of coastal Sumatra weather. They further concluded that the offshore migration of the diurnal cycle peaks was distinct (indistinct) when the MJO was over the Indian Ocean (had passed Sumatra), similar to the findings from Kamimera et al. [47], indicating that the modulations from the Indian Ocean might play critical roles. These proposed phenomena require detailed analysis, including a comparison of dominating factors among different MJO stages. Besides, the gravity wave signal, as one mechanism of the offshore rainfall migration, was found evident even after the MJO active stage when there was little precipitation, as reflected in the study in New Guinea from Vincent and Lane [23].

Unlike most of the prior studies, the present study is to compare the multi-scale influences of MJO on diurnal rainfall variation and associated offshore propagation among different MJO phases, near the western coast of Sumatra during the boreal winter seasons (December, January, and February) of the latest 10 years (2011–2020). To achieve this goal, the diurnal rainfall variations among different MJO phases are compared from perspectives of large-scale backgrounds and local-scale land–sea circulations associated with gravity waves. The rest of the paper is organized as follows. Section 2 introduces the data and methodology used in this study. Section 3.1 describes the spatial and temporal variations of rainfall during different MJO phases. The effects of large-scale circulations and local-scale land–sea circulations are analyzed in Sections 3.2 and 3.3, respectively. Section 3.4 explores the mechanisms of offshore diurnal propagation and its relationship with MJO. Finally, Section 4 presents a discussion and Section 5 summarizes the conclusions.

2. Data and Methodology

The coastal area around western Sumatra was selected as the analysis region in the present paper (Figure 1a). The Barisan Mountains lie along the west coast of Sumatra, with the highest elevation of around 1.5 km above mean sea level (AMSL). Figure 1b presents the vertical cross section of topography perpendicular to the Barisan Mountains averaged over the red box in Figure 1a.

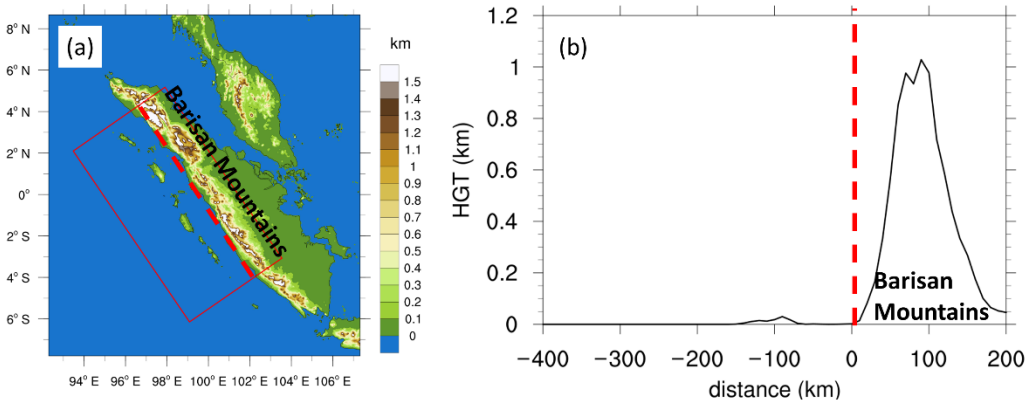

Figure 1. (**a**) The spatial distribution and (**b**) the vertical cross section (perpendicular to the coast) of topography (km) near western Sumatra coast. The red solid box is used for all the Hovmöller diagrams in this paper, with the distance ranging from −400 km offshore to 200 km onshore. The red dashed line marks the location of western coast with the distance of 0 km in (**b**).

The 0.1° × 0.1° Integrated Multi-satellitE Retrievals for GPM (IMERG) V06B final run precipitation data [52,53] was used to present the rainfall distribution and its diurnal variation. A comparison among different products (early run, late run and final run) indicated very limited differences between one another, and the final run data was utilized subsequently, with the consideration that it underwent additional adjustments with gauge data and climatology, compared with the early run or late run products. The half-hourly IMERG data was combined each hour to estimate the hourly precipitation rate. The 0.25° × 0.25° ECMWF Reanalysis 5th Generation (ERA5) data [54] during winter seasons (month DJF) of 2011–2020 was adopted for the background circulation analysis. The hourly ERA5 data began at 1000 hPa with the largest vertical interval of 50 hPa in the upper half of the troposphere.

The daily real-time multivariate MJO (RMM) index provided by the Australian Government Bureau of Meteorology is utilized to identify MJO phases, was calculated with outgoing long-wave radiation and 850-hPa/200-hPa zonal wind within 15° N–15° S, based on the method from Wheeler and Hendon [55]. The MJO amplitude was estimated using the RMM1 and RMM2 series generated by the empirical orthogonal functions (EOF) analysis. An MJO amplitude exceeding 1.0 indicates a strong MJO event. The MJO phases ranging from P1 to P8 correspond to varying locations of the active tropical convective disturbance: western hemisphere and Africa in P8–P1P8–P1, Indian Ocean in P2–P3, MC in P4–P5, and western Pacific Ocean in P6–P7. The days during strong MJO events in DJF 2011–2020 were classified into these four groups.

3. Results

3.1. Rainfall Variations Modulated by MJO

3.1.1. Spatial Distribution

Figure 2 shows the spatial distribution of the precipitation rate averaged in DJF 2011–2020 and the rainfall anomalies in different MJO phases. The islands of Sumatra, Borneo and Java, together with adjacent seas, had the highest precipitation rate of above 0.4 mm h^{-1} due to the windward side of MC (Figure 2a). The locations of positive rainfall anomalies are consistent with the MJO convective disturbances among different MJO

phases found in previous studies [43,46]. The rainfall anomalies in our analysis region (green box) and surrounding environments are consistently positive in P2–P3 (Figure 2c) and negative in P6–P7 (Figure 2e), which corresponds to the active phase and the suppressed phase, respectively, that are significantly affected by the large-scale background circulation associated with the MJO (which will be discussed in Section 3.2). In contrast, the rainfall anomalies in P8–P1P8–P1 are positive near the coastal region of Sumatra but are negative in the surrounding areas; P4–P5 exhibits opposite characteristics of the drier coast and the wetter environment. Both P8–P1 and P4–P5 are transitional phases between the active phase (P2–P3) and the suppressed phase (P6–P7), suggesting the lower impacts of MJO convective disturbances and indicating other possible factors that might take the lead (which will be discussed in Section 3.3).

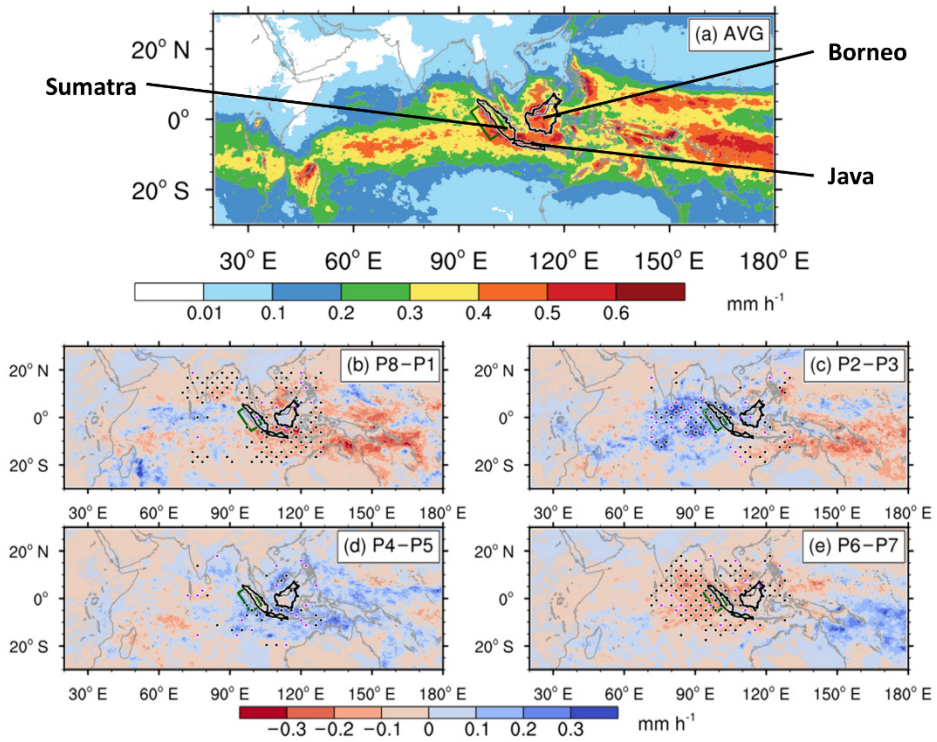

Figure 2. The precipitation rate (mm h^{-1}) (**a**) averaged in DJF 2011–2020 and its anomalies in (**b**) P8–P1, (**c**) P2–P3, (**d**) P4–P5 and (**e**) P6–P7. The black outlines mark the islands of Sumatra, Borneo and Java. The green box at western Sumatra coast marks the analysis region in this paper. The purple and black dots indicate the 90% and 95% confidence at 20° N–20° S, 70° E–130° E, according to the Student's *t*-test.

3.1.2. Diurnal Variation

Figure 3 contains the Hovmöller diagrams of precipitation rates among different MJO phases. In general, the diurnal variation of coastal rainfall stands out with a daytime landside peak followed by a nighttime seaside peak. The diurnal amplitude varies among different MJO phases, as strongest in P2–P3 (Figure 3b) and weakest in P6–P7 (Figure 3d), similar to the findings from Fujita et al. [46]. The diurnal variation of rainfall is characterized by evident offshore propagation, relatively obscured in P4–P5 (Figure 3c). The landside rainfall begins around 1300 LST around 50 km onshore, and migrates offshore with a phase speed of 3–4 m s^{-1}, until approximately ~30 km offshore around 0100 LST. Subsequently, the offshore propagation with a higher phase speed of 8–9 m s^{-1} occurs from ~30 km offshore to ~300 km offshore until ~1000 LST in the following day. In P4–P5, a diurnal phase-locking pattern with a maximum at ~0600 LST is found around −370–−160 km offshore.

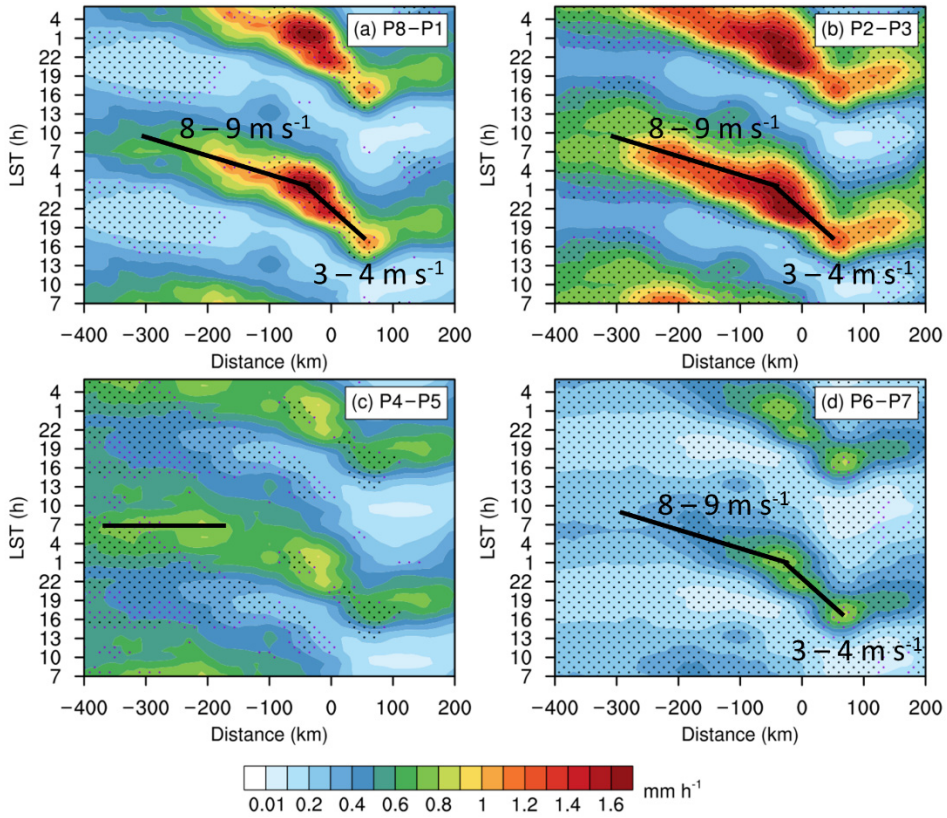

Figure 3. The time-distance Hovmöller diagrams of hourly precipitation rate (mm h^{-1}) in (**a**) P8–P1, (**b**) P2–P3, (**c**) P4–P5 and (**d**) P6–P7 averaged in DJF 2011–2020. The purple and black dots indicate the 90% and 95% confidence according to the Student's *t*-test.

In addition to the absolute diurnal amplitudes described above, we compare the relative diurnal amplitudes. Figure 4 includes the Hovmöller diagrams of normalized hourly precipitation deviation, which is calculated as the ratio of diurnal deviation to daily mean in each MJO stage. Although the absolute diurnal amplitude in P2–P3 is slightly higher than that in P8–P1 (Figure 3), the relative diurnal amplitude in P2–P3 is much lower than that in P8–P1 (Figure 4). Similar features exist in the comparison of P4–P5 and P6–P7. The sinusoidal regression averaged within −100–0 km from the coast quantitatively achieves the offshore absolute diurnal amplitudes (A_o) and normalized diurnal amplitudes (A_n), as displayed in Table 1. The A_o in P2–P3 is much higher than that in P6–P7 due to the significant large-scale contrast of the wettest and driest stages in MJO, but A_n becomes similar in the two stages due to the strengthened diurnal signal in P6–P7, which is also available in P8–P1, in which A_n is much higher than that in P4–P5. The ratio R_a, calculated as A_o divided by A_n is also exhibited, representing hourly precipitation rates (mm h^{-1}) averaged within −100–0 km offshore. Furthermore, R_a indicates larger difference between P8–P1 and P2–P3 as well as between P4–P5 and P6–P7 than A_o does, because A_o is the product of R_a and A_n for which the features contrast each other. For example, R_a is higher in P2–P3 (active stage) than in P8–P1 (transitional stage), while A_n is in the opposite possibly due to local effects, but their difference in A_o is relatively minor. The comparison of R_a better reflects the influences from the large-scale background circulation associated with MJO, than that of A_o.

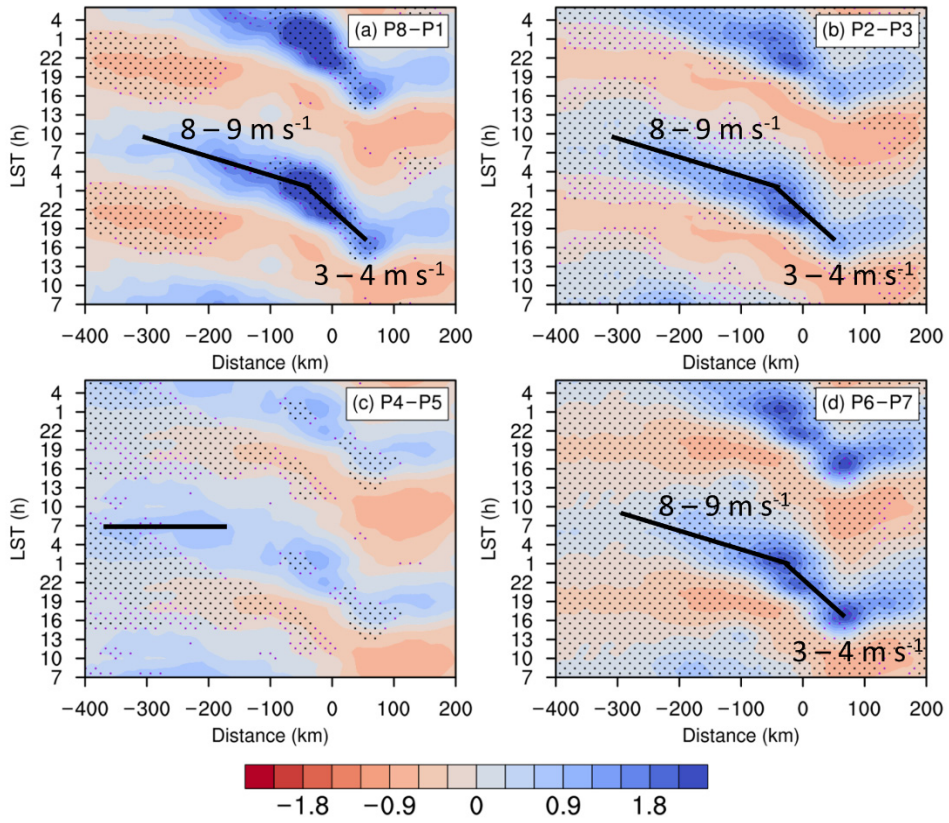

Figure 4. As in Figure 3 but for normalized hourly precipitation deviation in (**a**) P8–P1, (**b**) P2–P3, (**c**) P4–P5 and (**d**) P6–P7 averaged in DJF 2011–2020.

Table 1. Diurnal amplitudes from precipitation (A_o, mm h^{-1}) and from normalized precipitation (A_n) averaged within −100–0 km offshore via sinusoidal regressions, together with R_a (mm h^{-1}) calculated as A_o divided by A_n.

	P8–P1	P2–P3	P4–P5	P6–P7
$\mathbf{A_o}$	0.599	0.648	0.248	0.266
$\mathbf{A_n}$	0.896	0.799	0.491	0.762
$\mathbf{R_a}$	0.668	0.812	0.505	0.349

3.2. Effect of Large-Scale Forcing

Based on the characteristics in Section 3.1, the large-scale background circulations among different MJO phases are compared. Figure 5a shows the seasonal mean of zonal winds and vertical motions at 850-hPa, whereby the upward motions are marked with diagonal lines. The westerly winds from northern Indian Ocean, and the northeasterly winds from the north of Borneo, bring abundant oceanic moisture and converge at the western Sumatra coast. The upward motions dominate at and around the coast. Both the thermodynamic and dynamic conditions are favorable for coastal rainfall, consistent with the high rainfall rate indicated in Figure 2a.

Figure 5b–e present the anomalies of zonal winds and vertical motions at 850 hPa under different MJO phases, where the positive (upward) anomalies are marked with diagonal lines. In P2–P3 (Figure 5c), the strengthened westerly winds to the west and the strengthened easterly winds to the northeast result in the stronger convergence near the Sumatra Island, while the wind anomalies in P6–P7 exhibit an opposite scenario and weakened convergence. In addition, the vertical motions near the Sumatra Island in P2–P3 are much stronger than that in P6–P7, while the anomalies of 850-hPa water vapor mixing ratio in P2–P3 (P6–P7) are positive (negative) near the Sumatra Island (Figure 6b,d), further

influencing the strength of moist advection and convection (Figure 2b–e). The results above could explain why P2–P3 and P6–P7 are the wettest and driest MJO stages at Sumatra.

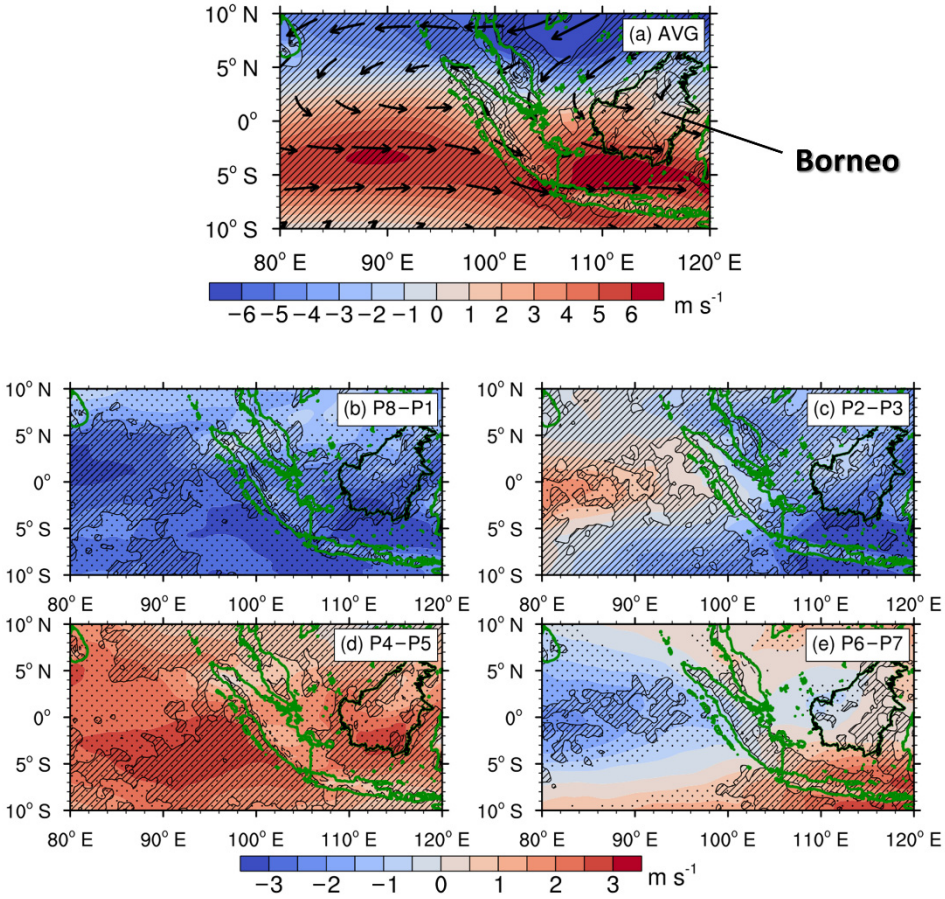

Figure 5. The horizontal distributions of zonal wind (shaded, m s^{-1}) and vertical motions (contour, 0.5 cm s^{-1}) at 850 hPa (**a**) averaged in DJF 2011–2020 as well as its anomaly in (**b**) P8–P1, (**c**) P2–P3, (**d**) P4–P5 and (**e**) P6–P7. The black outline marks the island of Borneo. The diagonal lines indicate the positive (upward) averages or phase anomalies for vertical motions. The black dots indicate the 95% confidence according to the Student's *t*-test.

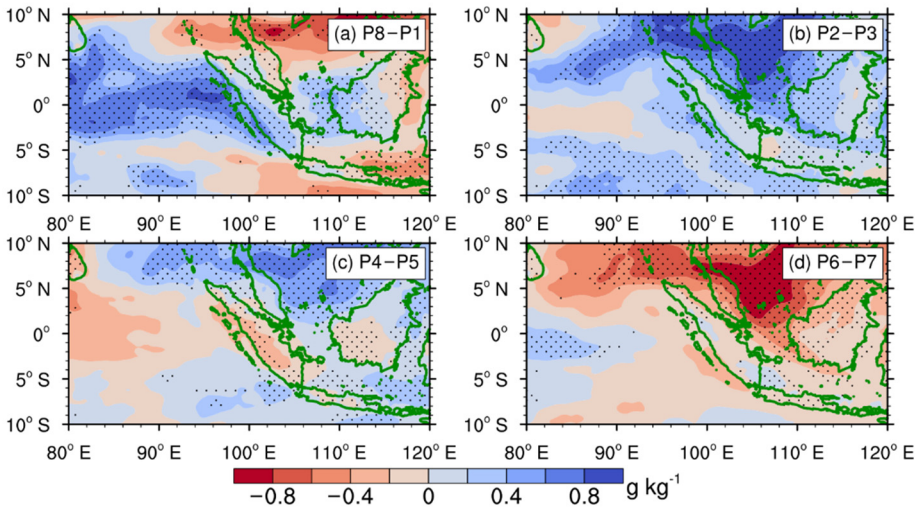

Figure 6. The anomalies of water vapor mixing ratio at 850 hPa (g kg^{-1}) in (**a**) P8–P1, (**b**) P2–P3, (**c**) P4–P5 and (**d**) P6–P7. The black dots indicate the 95% confidence according to the Student's *t*-test.

In contrast, P8–P1 and P4–P5 have both conducive and unconducive conditions affecting the convection. As shown in Figure 5b,d, the wind anomalies to the west and northeast of Sumatra are consistent, and result in relatively weaker convergence anomalies. The differences in the precipitation rate (higher in P8–P1 than in P4–P5) arise mostly from the upstream vapor anomalies at the northern Indian Ocean (Figure 6a,c).

Therefore, the large-scale conditions for precipitation are favorable in the active stage P2–P3, unfavorable in the suppressed stage P6–P7, and relatively neutral in the transitional stages P8–P1 and P4–P5, influenced largely by local factors.

3.3. Effect of Local-Scale Land-Sea Circulation

Figure 7 presents the anomalies of total cloud cover under different MJO phases, which is in agreement with the precipitation anomalies (Figure 2). The cloud cover anomalies may lead to a variation in the normalized diurnal precipitation amplitude (A_n) among different MJO phases by modulating the land–sea thermal contrast and the local-scale land–sea circulation via the solar radiative heating: less cloud leads to higher thermal contrast and stronger local circulation via enhanced radiative heating. The absolute diurnal precipitation amplitude (A_o) and the coastal precipitation rate (R_a) in P6–P7 are much lower than those in P2–P3, but the normalized diurnal precipitation variation amplitudes (A_n) become similar in the two stages (Table 1) due to the lower cloud cover in P6–P7 (Figure 7). Similarly, A_o and R_a are lower in P8–P1 than in P2–P3, but A_n is higher in P8–P1 with less cloud. Therefore, the diurnal rainfall signals are influenced not only by large-scale background conditions but also by local-scale radiative heating or cooling, where the cloud cover plays a nonnegligible role, as indicated by previous studies [34,45,56–60].

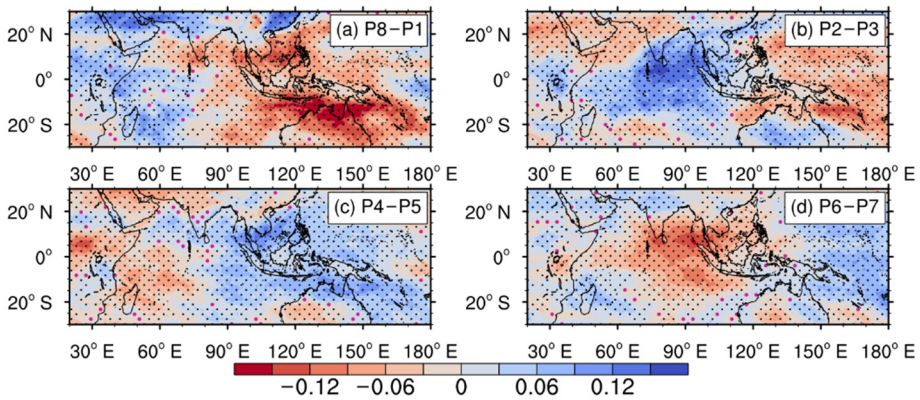

Figure 7. As in Figure 6 but for the anomalies of total cloud cover in (**a**) P8–P1, (**b**) P2–P3, (**c**) P4–P5 and (**d**) P6–P7. The purple and black dots indicate the 90% and 95% confidence according to the Student's *t*-test.

Figure 8 compares the diurnal variations (Figure 8a) and diurnal amplitudes (Figure 8b) of land–sea temperature contrast at 850 hPa, as the driving factor of land–sea circulation, among different MJO phases. The daytime positive temperature contrast (warmer on land) and the nighttime negative temperature contrast (warmer over ocean), as presented in Figure 8a, derives from the radiative heating and cooling influenced by relatively lower landside heat capacity. The time series in P8–P1 are very close to the total average, which is a possible explanation for the insignificance through the *t* test. The diurnal variation is strongest in P6–P7 and weakest in P2–P3 (Figure 8b). As is known, low-level temperature is modulated largely by cloud cover and precipitation. In P6–P7 the cloud cover is lowest (Figure 7d), leading to most of the apparent daytime radiative heating and nighttime cooling (Figure 8a), meanwhile P6–P7 is also the driest stage due to its divergence anomalies (Figure 5e) and negative moisture anomalies (Figure 6d) so that the daytime precipitation cooling over the land is weakest, further enlarging the diurnal amplitude (Figure 8b). In contrast, the higher cloud cover in P2–P3 (Figure 7b) lowers the radiative heating

and increases the daytime landside precipitation cooling, both resulting in the weakened diurnal temperature variation (Figure 8b). In other words, the radiative modulation and precipitation cooling are both conducive (unconducive) for enlarging the diurnal temperature amplitude in P6–P7 (P2–P3), so the distinction between these two stages is most evident. Similar features are reflected via the comparison between P8–P1 and P2–P3 as well as between P4–P5 and P6–P7. Note that the difference between P8–P1 and P4–P5 is minor where the conducive and unconducive conditions are mixed: the stronger cloud-affected radiative modulation is more favorable for the diurnal temperature variations in P8–P1, but the weaker landside precipitation cooling is more favorable in P4–P5.

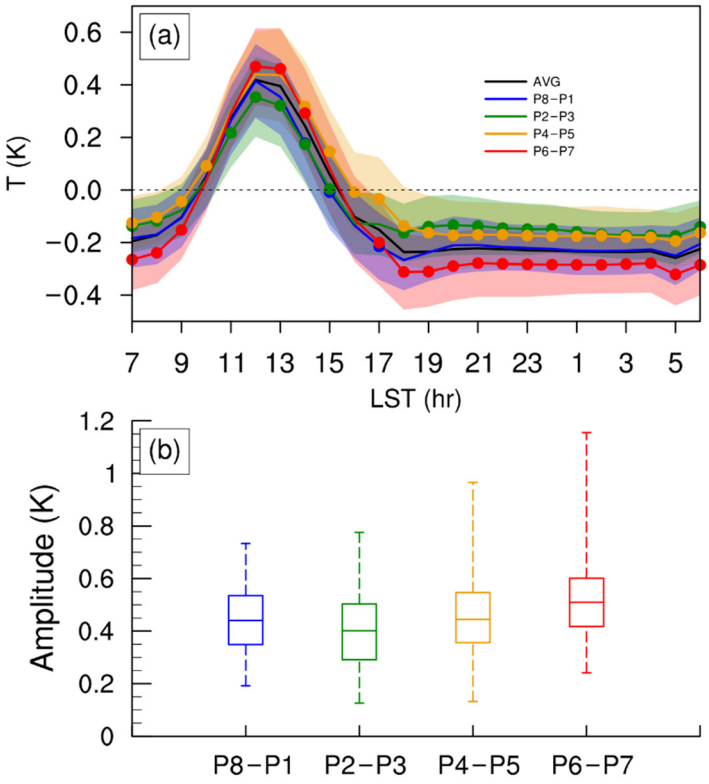

Figure 8. (**a**) The diurnal variations of 850-hPa land–sea temperature contrast (line, K) and its standard deviation (shaded, K) for total average and phase averages, calculated as the landside mean subtracted by seaside mean within 100 km from western Sumatra coast; (**b**) the box figures of diurnal amplitudes (K). The dots in Figure 8a indicate the 95% confidence according to the Student's *t*-test.

Figure 9 compares the diurnal variations of low-level land–sea circulations by presenting the differences between the vertical circulation at 0100 LST and at 1300 LST. The seasonal mean land–sea nocturnal circulation (Figure 9a) reveals upward motions over the ocean and downward motions over the land, with a distinct boundary close to the western Sumatra coast. The cloud cover had a noticeable impact below 1.5 km AMSL, and the P8–P1 and P6–P7 stages with lower cloud cover had enhanced land–sea circulations (Figure 9b,e), whereas the higher cloud cover in P2–P3 and P4–P5 compressed the land–sea circulations (Figure 9c,d), consistent with the higher (lower) 850-hPa diurnal temperature amplitudes in P8–P1 and P6–P7 (P2–P3 and P4–P5) (Figure 8), revealing the dependency of land–sea circulation on the diurnal land–sea thermal contrast. The boundaries between positive and negative vertical motion anomalies near the coast are clearer in the transitional MJO phases, P8–P1 and P4–P5, reflecting larger impacts of cloud cover on the local-scale circulation and the diurnal variation of precipitation in these phases. The consistently (both seaside and landside) positive (negative) vertical motion anomalies near the coast, of above 1.5 AMSL in P2–P3 (P6–P7) reflect the dominating modulations by the large-scale MJO circulations.

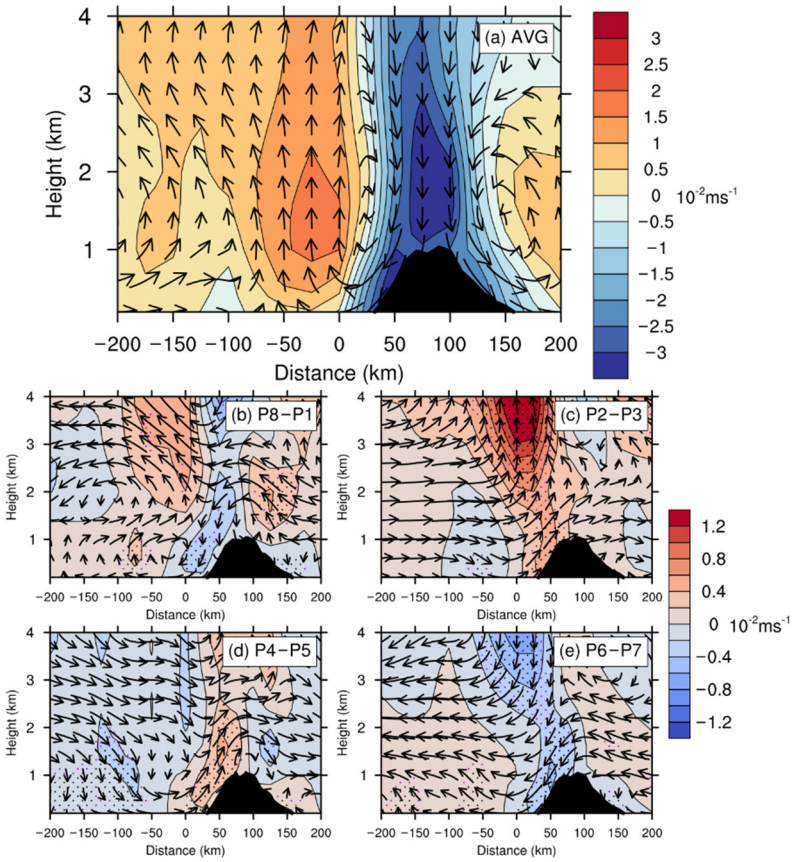

Figure 9. The differences of vertical motion (shaded, 10^{-2} m s^{-1}, positive means upward) and wind vectors (the horizontal wind normal to western Sumatra coast with the vertical motion) at 0100 LST from those at 1300 LST (**a**) averaged in DJF 2011–2020 as well as its anomaly in (**b**) P8–P1, (**c**) P2–P3, (**d**) P4–P5 and (**e**) P6–P7. The black shade marks the topography of coastal mountains. The purple and black dots indicate the 90% and 95% confidence according to the Student's *t*-test.

The positive middle-level offshore vertical motion anomalies in the diurnal circulation enhance the nighttime offshore convection and enlarge the diurnal offshore variation both in P8–P1 and P2–P3 (Figure 9b,c), but their mechanisms might be different. In P8–P1, the stronger offshore convection is driven by the strengthened offshore transportation of upward motions from coastal topography (stronger gravity waves), attributed to a greater land–sea contrast of low-level temperature arising from enhanced cloud-affected radiative heating. In P2–P3, however, such offshore gravity waves are less evident due to relatively weaker radiative heating and stronger daytime precipitation cooling over the land. Nevertheless, the enhanced low-level onshore background wind and its convergence with local land surges contribute to the stronger offshore convection in P2–P3. In other words, the normalized diurnal precipitation variation in P8–P1 takes larger effects from the local-scale circulations (or gravity waves) under the cloud cover modulations, while the large-scale backgrounds play more important roles in P2–P3. Similar characteristics are revealed in the comparison between P4–P5 and P6–P7.

3.4. Diurnal Propagation Associated with Gravity Waves

As shown in Figures 3 and 4, the average phase speed of diurnal offshore precipitation propagation is 3–4 m s^{-1} near the coast, similar with the magnitudes in the land breeze or the cold pool outflow [28,30,32,61]. The phase speed of 8–9 m s^{-1} further offshore is noticeably distinguished from the magnitude of background wind, and indicates other possible factors such as gravity waves, with a similar speed of roughly 8–15 m s^{-1}, as generated by land–sea thermal contrast or convection [21,24,62–65]. The mechanism of this quicker propagation affecting the diurnal rainfall farther offshore will be explored

in this section. Figure 10 shows the diurnal signals of offshore propagation in 700-hPa temperature by subtracting the spatial mean from the temporal deviations. The wavelike bands of positive signals (solid ellipses) and negative signals (dashed ellipses) parallel to the western Sumatra coast reflects the influences of the coastline as well as the coastal mountains on the temperature variations, similar with the findings from Ruppert and Zhang [66] as a horizontal view of geography-affected gravity wave activities. The landside positive band develops and is separated from the coast since 0700 LST; afterwards, it moves offshore and gradually dissipates to around 0700 LST the following day. The offshore migration speed from 1900 LST to 0400 LST is estimated to be about 9.7 m s^{-1}, similar to the magnitude of the precipitation migration from 0100 LST to 0700 LST which exhibits a phase lag of approximately 6 h. The landside rainfall is evident since 1600 LST, after the strong thermal convection and the cloud formation around 1300 LST. The offshore migration of rainfall begins at 2200 LST when the thermal disturbance moves offshore, and this migration sustains until 1000 LST in the next day, similar to the beginning and ending of the migration exhibited in Figures 3 and 4.

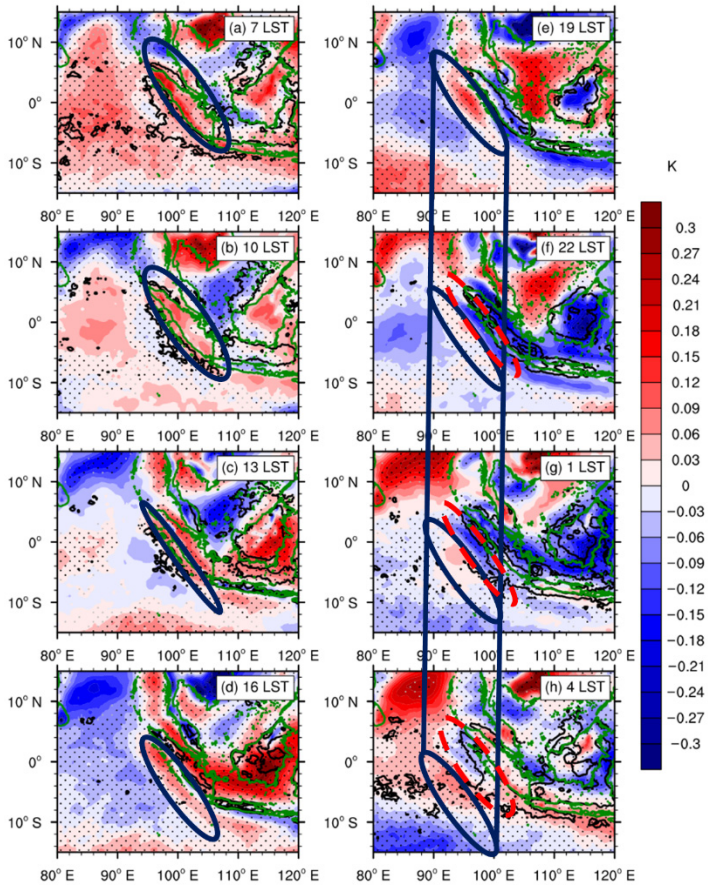

Figure 10. The diurnal variation of 700-hPa temporal temperature disturbance (K) with spatial mean subtracted (shaded) as well as precipitation rate (contour, interval 0.5 mm h^{-1}), as averaged at (**a**) 07 LST, (**b**) 10 LST, (**c**) 13 LST, (**d**) 16 LST, (**e**) 19 LST, (**f**) 22 LST, (**g**) 01 LST, and (**h**) 04 LST, in DJF 2011–2020. The local standard time (LST) is calculated with a Coordinated Universal Time (UTC) offset of +7. The solid (dashed) ellipses mark the positive (negative) signals. The grey and black dots indicate the 90% and 95% confidence according to the Student's *t*-test.

The vertical structures of the wavelike signals are presented in Figure 11. The land–sea contrast of daytime radiative heating induces the low-level landside warm disturbance (Figure 11b–d), of which the vertical structure tilts to the offshore side at 1300 LST (Figure 11c). Then, this vertically tilted phase line (or ray path) propagates offshore and downward until 2200 LST (Figure 11d–f). Meanwhile, the cool tilted disturbance from

landside radiative cooling forms at night and repeats the offshore migration (Figure 11e–h). These warm and cool tilted disturbances might come from the gravity waves driven by diurnal land–sea thermal contrast [29,63,64,67]. The offshore low-level warm disturbance and midlevel cool disturbance (Figure 11e–h) helps to destabilize the local atmosphere and creates more conducive environments for the nighttime development of offshore convection. Those patterns are in general agreement with the vertical structures in the study of Bai et al. [65]. The continuous propagation of warm and cool signals until 0700 LST on the next day are considered a main factor of the offshore rainfall migration, with the phase speeds (peak values) estimated as 9.3 m s^{-1} at 900 hPa and 11.6 m s^{-1} at 600 hPa.

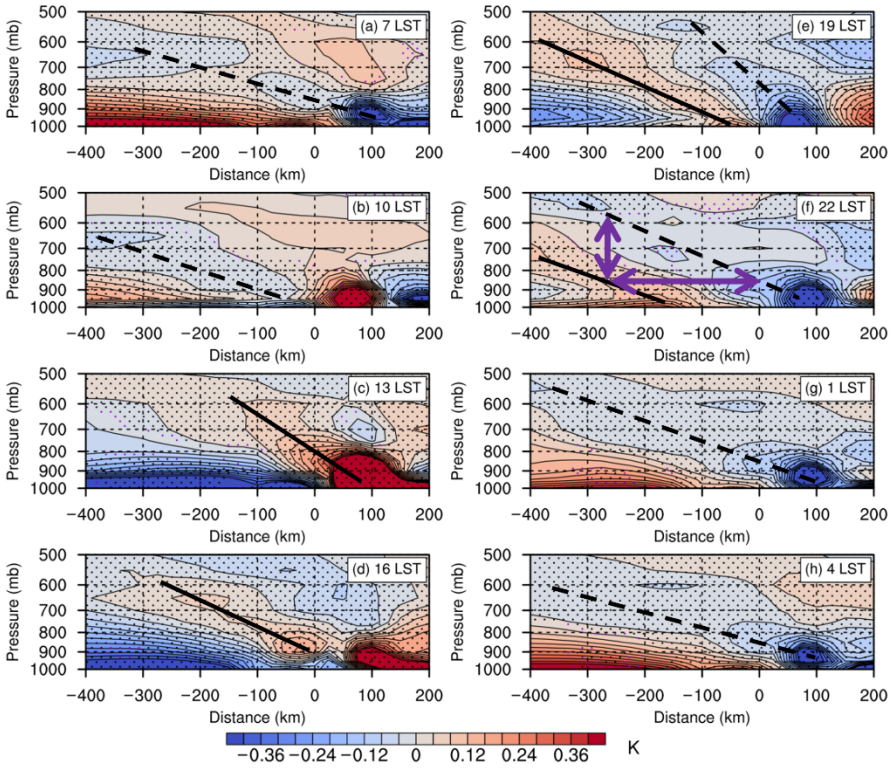

Figure 11. The temporal evolution of the vertical cross section of temperature deviations (K) as averaged at (**a**) 07 LST, (**b**) 10 LST, (**c**) 13 LST, (**d**) 16 LST, (**e**) 19 LST, (**f**) 22 LST, (**g**) 01 LST, and (**h**) 04 LST, in DJF 2011–2020. The purple and black dots indicate the 90% and 95% confidence according to the Student's *t*-test.

The phase speed c of offshore migration (precipitation or temperature disturbance) was estimated as the speed of peak values, as well as with the dispersion relation included in the study from Du and Rotunno [63] as follows:

$$c = \frac{\omega}{k} \quad (1)$$

$$\omega = \sqrt{f^2 + N^2 \frac{k^2}{m^2}} \quad (2)$$

where ω is the frequency, k and m is the dominant horizontal and vertical wavenumber, f is the Coriolis parameter, and N is the buoyancy frequency. According to the utilized ERA5 reanalysis data in our study region, $f \approx 5.2 \times 10^{-6}$ s^{-1} and $N \approx 0.012$ s^{-1}. The leaning vertical structure of the gravity waves in Figure 11f exhibits the horizontal and vertical wavelength to be approximately 500 km and 3.3 km (marked with purple vectors), while the corresponding wavenumber is $k \approx 1.26 \times 10^{-5}$ m^{-1} and $m \approx 9.52 \times 10^{-4}$ m^{-1}. Hence, the phase speed (dispersion relation) was estimated as roughly 12.6 m s^{-1}. These

estimations are close to those of precipitation far offshore in Figures 3 and 4 (8–9 m s^{-1}), as well as with the estimates in existing literature mentioned at the beginning of this section. The horizontal wavelength of ~500 km suggests the gravity waves in this study to be meso-large-scale.

The differences in the gravity wave signals among various MJO phases and their influences on coastal rainfall propagation are also compared. Figure 12 presents the Hovmöller diagrams of differences between 850-hPa and 600-hPa temperature, as the index of low-level thermal instability. This index also reflects the modulations of the wavelike signals associated with gravity waves, as exhibited in Figure 11. The landside instability increases with accumulated radiative heating and reaches its maximum at around 1300 LST, after which it propagates offshore and destabilizes the seaside atmosphere as the gravity waves propagate offshore. The increased offshore thermal instability contributes to the convection development. The increasing offshore precipitation rate before its peak is accompanied by the positive diurnal deviation of the thermal instability, and their orthogonal relation indicates a phase lag of 6–9 h. The rainfall rate then reaches its peak shortly before the offshore thermal instability (Figure 12a) falls onto the daily mean.

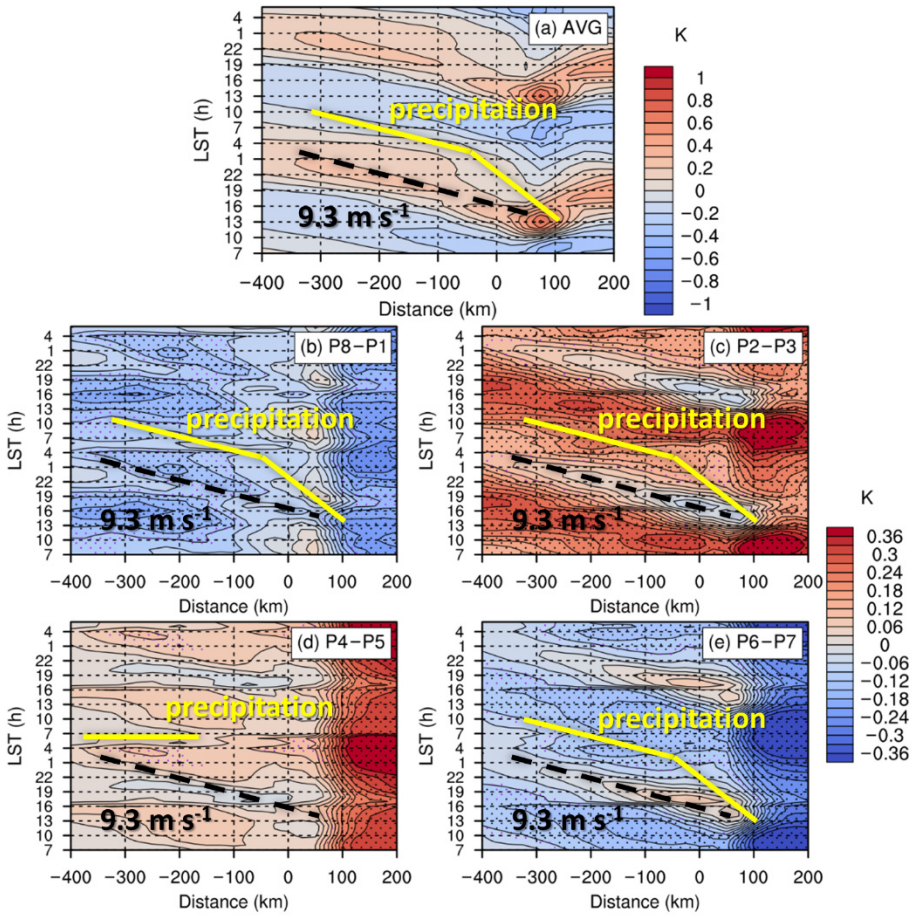

Figure 12. The Hovmöller diagrams of temperature difference (K) between 850 hPa and 600 hPa (**a**) averaged in DJF 2011–2020 with daily mean subtracted, as well as its anomaly in (**b**) P8–P1, (**c**) P2–P3, (**d**) P4–P5 and (**e**) P6–P7. The black dashed lines mark the daily maximum of temperature difference in (**a**). The yellow solid lines mark the diurnal maximum of precipitation as indicated in Figure 3. The purple and black dots indicate the 90% and 95% confidence according to the Student's *t*-test.

The positive anomalies of low-level thermal instability generally dominate in P2–P3 and P4–P5 (Figure 12c,d) with the higher cloud cover (Figure 7). Since the 850-hPa temperature is lowered, owing to the weaker radiative heating during these stages, the higher

vertical temperature gradient should result from the larger decrease of 600-hPa temperature. The larger fraction of cloud that is apparently colder than the surrounding 600-hPa air noticeably lowers the average temperature, and vice versa in P8–P1 and P6–P7 (Figure 12b,e) with lower cloud fraction. As revealed in the averaged diurnal cycle (Figure 12a), the offshore migration of warm disturbance as the signals of gravity waves causes the increase in low-level instability along the track of migration. The lowered differences between diurnal peaks and daily averages in P2–P3 and P4–P5 (Figure 12c,d) indicates weakened gravity wave signals, due to the suppressed land–sea thermal contrast under the lowered radiative heating owing to the thicker cloud. In contrast, the thinner cloud in P8–P1 and P6–P7 (Figure 12b,e) is conducive to enhancing the land–sea thermal contrast as well as the associated gravity-wave signals via radiative heating, as indicated by the enhanced differences between diurnal peaks and daily averages, and therefore, has positive effects on the diurnal rainfall variation, consistent with the noticeably high normalized diurnal variation amplitudes A_n exhibited in Table 1.

In addition to the weakened gravity waves, P4–P5 is the only stage with apparently strengthened westerly wind on the upstream side (Figure 5), which also possibly prevents the offshore migration of precipitation during this stage, and thus leads to the phase-locking pattern of diurnal precipitation off the western coast (Figures 3 and 4).

4. Discussion

The noticeable difference between precipitation rates at the western Sumatra coast and its surroundings, as revealed in Figure 2, was also exhibited in the study by Peatman et al. [43]. They mentioned the non-zero or positive precipitation anomalies over Sumatra in MJO P1, defined by Wheeler and Hendon [55] whereby negative anomalies dominated MC, meanwhile, the diurnal amplitudes of precipitation reflected similar features with the absolute diurnal amplitude A_o in our Table 1. Other previous studies indicate prominent diurnal rainfall cycles and offshore migrations at or around P2–P3, with an MJO active convection at the northern Indian Ocean [36,46,47], also in agreement with our findings. Nevertheless, these studies hardly focus on normalized diurnal variation amplitudes (equally A_n in our Table 1), including the higher A_n in P8–P1 than P2–P3, as well as the relatively high A_n in the driest stage P6–P7. The study from Sakaeda et al. [39] exhibits an inconsistency between absolute amplitudes and normalized amplitudes of diurnal coastal precipitation variation, while we further compared this inconsistency during different MJO phases. A comparison and analysis of A_o and A_n among different MJO phases in this study, is expected to further acknowledge the detailed influences of the MJO on the diurnal precipitation cycle.

Various-scale factors for the diurnal rainfall cycle, as indicated within the existing literature introduced in the introduction, usually coexist with one another. This study further focuses on answering the question, that how these factors affect the coastal precipitation during different MJO phases. According to the analysis in Sections 4 and 5, the large-scale impacts of background wind and moisture on the absolute diurnal amplitude dominate during the MJO active (P2–P3) or suppressed (P6–P7) phases at Sumatra, while the modulations of the local-scale land–sea circulation influencing normalized diurnal amplitude are more distinct during the transitional phases (P8–P1 and P4–P5).

In terms of the offshore propagation, several studies [23,29,31] presented distinguished migration near and farther away the coast, whose speeds and ranges are close to those in this study. The wavelike signals (Figure 10) and the leaning vertical structures (Figure 11), generated from local land–sea thermal contrast, resemble the features of gravity waves in existing studies [65,66]. The variation among different MJO phases (Figure 12) reveals the consistency of lower cloud cover (Figure 7) with stronger gravity waves, according to the modulation of radiative heating and cooling. On the other hand, the strengthened waves are not always related with apparent rainfall migration. According to our analysis, the gravity waves were relatively weak in P2–P3, but the environment was dominated by enhanced vertical vapor transportation due to low-level high moisture, as found critical

for offshore precipitation in the research from Du and Rotunno [64], and hence is dynamically (convectively) favorable for the coupling of gravity waves and convection [68,69]. That is a possible reason for the strong offshore rainfall propagation in P2–P3, with the noticeable diurnal rainfall cycle (both A_o and A_n in Table 1). In contrast, the environment is thermodynamically (radiatively) favorable for the strength of gravity waves both in P8–P1 and in P6–P7, with higher (similar) diurnal amplitude of normalized precipitation (A_n) in P8–P1 (P6–P7) compared to that in P2–P3, partly similar with the findings from Vincent and Lane [23]. However, the diurnal offshore migration is relatively (noticeably) weaker in P8–P1 (P6–P7), probably owing to weaker vertical vapor transportation and associated coupling with gravity waves compared to P2–P3. Consequently, the coupling (decoupling) of local thermal gravity waves and convection, under the positive (negative) large-scale synoptic modulation, was considered the main factor for the evident (obscured) diurnal offshore rainfall propagation in P2–P3 (P6–P7). In one word, the gravity waves are from local-scale land–sea thermal contrast but its coupling depends greatly on large-scale moisture and convection, both of which influence the coastal precipitation but reveal unique features during each MJO phase. To summarizr, this study not only compares the diurnal variation, especially the associated offshore migration, of winter rainfall among various MJO phases, but also analyzes the large-scale and local-scale impacts which play varying roles during different MJO phases.

5. Conclusions

This paper focused on the influences of winter MJO on the diurnal rainfall variation and its offshore propagation near western coast of Sumatra during 2011–2020 using ERA5 reanalysis. Days under strong MJO background were separated into four stages according to the locations of convective disturbance, respectively, at western hemisphere in P8–P1, at Indian Ocean in P2–P3, at MC in P4–P5, and at western Pacific Ocean in P6–P7. Features that relate to precipitation daily mean rates, diurnal variations, normalized diurnal variations and offshore diurnal propagation were compared among different MJO stages and were explained using an analysis of both large-scale backgrounds and local-scale land–sea circulation. The conclusions are summarized as follows:

More (Less) precipitation occurs near the coastal area in P8–P1 and P2–P3 (P4–P5 and P6–P7); specifically, in P2–P3 (P6–P7) the precipitation is both enhanced (suppressed) at the coastal area and its surroundings, while in P8–P1 the coastal enhancement is accompanied by the surrounding suppression, and vice versa in P4–P5. Precipitation rates and their absolute diurnal variations are affected greatly by large-scale backgrounds. The low-level convergence and moisture are both favorable (unfavorable) in P2–P3 (P6–P7), producing the most (least) rainfall. The moisture in the northern Indian Ocean plays a critical role in affecting precipitation rates during other stages (P8–P1 and P4–P5) where the large-scale low-level convergence is not favorable as in P2–P3.

Normalized precipitation diurnal variations are not consistent with absolute diurnal variations among different MJO phases. The normalized diurnal amplitude is higher in P8–P1 compared to the P4–P5, arising largely from the enhanced diurnal land–sea circulation variations. Although the absolute diurnal amplitude in P2–P3 is much stronger than P6–P7 due to large-scale MJO circulation, the normalized diurnal amplitude in P6–P7 resembles that in P2–P3, suggesting that the strength of the land–sea diurnal circulation plays an important role in the modulation of normalized diurnal amplitude, under the impact of cloud cover.

The offshore diurnal rainfall propagation is associated with gravity waves generated from land–sea thermal contrast by examining its phase speeds, horizontal wavelike signals as well as vertical structures in warm/cool disturbances. The wave signals are more explicit under lower cloud cover in P8–P1 and P6–P7, which is favorable for apparent diurnal propagation. The noticeable diurnal propagation in P2–P3, accompanied by weakened gravity wave signals, reflects the potential large-scale effects of vertical vapor transportation and the strong coupling of convection and gravity waves. The phase-locking diurnal pattern

off the coast in P4–P5 possibly occurs due to the local-scale seaside nighttime cooling of cloud top and the strong westerly. In P4–P5, the large-scale rainfall development is suppressed by weaker convergence and lower moisture meanwhile the local-scale land–sea circulation is prohibited by thicker cloud cover.

Since this paper focuses only on seasonal average precipitation during the past decade, in future studies, we plan to investigate specific cases, for the purpose of developing a better understanding of offshore migration and how it is influenced by the MJO. Numerical simulations as well as sensitivity experiments will also be conducted to verify and expanding our conclusions.

Author Contributions: Conceptualization, B.Z., Y.D. and Z.G.; methodology, B.Z. and Y.D.; data curation: Y.D.; software, B.Z. and Y.D.; validation, B.Z., Y.D. and Z.G.; formal analysis, B.Z. and Y.D.; writing—original draft preparation, B.Z.; writing—review and editing, B.Z., Y.D. and Z.G.; visualization, B.Z.; supervision, Y.D. and Z.G.; funding acquisition, Y.D. All authors have read and agreed to the published version of the manuscript.

Funding: The author Y.D. was supported by the Guangdong Major Project of Basic and Applied Basic Research (2020B0301030004), the National Natural Science Foundation of China (Grant Nos. 42075006, 42122033, and 41875055), and Guangzhou Science and Technology Plan Projects (202002030346).

Institutional Review Board Statement: Not applicable.

Informed Consent Statement: Not applicable.

Data Availability Statement: The IMERG precipitation data was from NASA's Global Precipitation Measurement Mission (https://gpm.nasa.gov/data/imerg; accessed on 10 February 2021). The ERA5 reanalysis data was obtained from NCEI (https://www.ncei.noaa.gov; accessed on 29 January 2021). The MJO RMM index data was from the Australian Bureau of Meteorology (http://www.bom.gov.au/climate/mjo/; accessed on 1 February 2021).

Acknowledgments: Computer support from the Center for High-Performance Computing at Nanjing University of Information Science & Technology is gratefully acknowledged. We sincerely thank all the editors and reviewers for the kind comments and valuable suggestions during the revisions.

Conflicts of Interest: The authors declare no conflict of interest.

References

1. Madden, R.A.; Julian, P.R. Detection of a 40–50 day oscillation in the zonal wind in the tropical Pacific. *J. Atmos. Sci.* **1971**, *28*, 702–708. [CrossRef]
2. Madden, R.A.; Julian, P.R. Description of global-scale circulation cells in the tropics with a 40–50 day period. *J. Atmos. Sci.* **1972**, *29*, 1109–1123. [CrossRef]
3. Zhang, C. Madden-julian oscillation. *Rev. Geophys.* **2005**, *43*, RG2003. [CrossRef]
4. Jeong, J.-H.; Kim, B.-M.; Ho, C.-H.; Noh, Y.-H. Systematic variation in wintertime precipitation in East Asia by MJO-induced extratropical vertical motion. *J. Clim.* **2008**, *21*, 788–801. [CrossRef]
5. Barrett, B.S.; Carrasco, J.F.; Testino, A.P. Madden–Julian oscillation (MJO) modulation of atmospheric circulation and Chilean winter precipitation. *J. Clim.* **2012**, *25*, 1678–1688. [CrossRef]
6. Juliá, C.; Rahn, D.A.; Rutllant, J.A. Assessing the influence of the MJO on strong precipitation events in subtropical, semi-arid north-central Chile (30 S). *J. Clim.* **2012**, *25*, 7003–7013. [CrossRef]
7. Zhou, S.; L'Heureux, M.; Weaver, S.; Kumar, A. A composite study of the MJO influence on the surface air temperature and precipitation over the continental United States. *Clim. Dyn.* **2012**, *38*, 1459–1471. [CrossRef]
8. Zhang, C.; Ling, J. Barrier effect of the Indo-Pacific Maritime Continent on the MJO: Perspectives from tracking MJO precipitation. *J. Clim.* **2017**, *30*, 3439–3459. [CrossRef]
9. Wang, B.; Rui, H. Synoptic climatology of transient tropical intraseasonal convection anomalies: 1975–1985. *Meteorol. Atmos. Phys.* **1990**, *44*, 43–61. [CrossRef]
10. Hartmann, D.L.; Michelsen, M.L.; Klein, S.A. Seasonal variations of tropical intraseasonal oscillations: A 20–25-day oscillation in the western Pacific. *J. Atmos. Sci.* **1992**, *49*, 1277–1289. [CrossRef]
11. Salby, M.L.; Hendon, H.H. Intraseasonal behavior of clouds, temperature, and motion in the tropics. *J. Atmos. Sci.* **1994**, *51*, 2207–2224. [CrossRef]
12. Wu, C.-H.; Hsu, H.-H. Topographic influence on the MJO in the Maritime Continent. *J. Clim.* **2009**, *22*, 5433–5448. [CrossRef]
13. Jia, X.; Chen, L.; Ren, F.; Li, C. Impacts of the MJO on winter rainfall and circulation in China. *Adv. Atmos. Sci.* **2011**, *28*, 521–533. [CrossRef]

14. Mori, S.; Hamada, J.-I.; Hattori, M.; Wu, P.-M.; Katsumata, M.; Endo, N.; Ichiyanagi, K.; Hashiguchi, H.; Arbain, A.A.; Sulistyowati, R. Meridional march of diurnal rainfall over Jakarta, Indonesia, observed with a C-band Doppler radar: An overview of the HARIMAU2010 campaign. *Prog. Earth Planet. Sci.* **2018**, *5*, 47. [CrossRef]
15. Katsumata, M.; Mori, S.; Hamada, J.-I.; Hattori, M.; Syamsudin, F.; Yamanaka, M.D. Diurnal cycle over a coastal area of the Maritime Continent as derived by special networked soundings over Jakarta during HARIMAU2010. *Prog. Earth Planet. Sci.* **2018**, *5*, 1–19. [CrossRef]
16. Ramage, C.S. Role of a tropical "maritime continent" in the atmospheric circulation. *Mon. Weather Rev.* **1968**, *96*, 365–370. [CrossRef]
17. Neale, R.; Slingo, J. The Maritime Continent and its role in the global climate: A GCM study. *J. Clim.* **2003**, *16*, 834–848. [CrossRef]
18. Chang, C.; Harr, P.A.; Chen, H.-J. Synoptic disturbances over the equatorial South China Sea and western Maritime Continent during boreal winter. *Mon. Weather Rev.* **2005**, *133*, 489–503. [CrossRef]
19. Lorenz, P.; Jacob, D. Influence of regional scale information on the global circulation: A two-way nesting climate simulation. *Geophys. Res. Lett.* **2005**, *32*, L18706. [CrossRef]
20. Ando, K.; Syamsudin, F.; Ishihara, Y.; Pandoe, W.; Yamanaka, M.D.; Masumoto, Y.; Mizuno, K. Development of new international research laboratory for maritime-continent seas climate research and contributions to global surface moored buoy array. In Proceedings of the "OeanObs' 09: Sustained Ocean Observations and Information for Society" Conference (Annex), Venice, Italy, 21–25 September 2009.
21. Mori, S.; Jun-Ichi, H.; Tauhid, Y.I.; Yamanaka, M.D.; Okamoto, N.; Murata, F.; Sakurai, N.; Hashiguchi, H.; Sribimawati, T. Diurnal land–sea rainfall peak migration over Sumatera Island, Indonesian Maritime Continent, observed by TRMM satellite and intensive rawinsonde soundings. *Mon. Weather Rev.* **2004**, *132*, 2021–2039. [CrossRef]
22. Love, B.S.; Matthews, A.J.; Lister, G.M. The diurnal cycle of precipitation over the Maritime Continent in a high-resolution atmospheric model. *Q. J. R. Meteorol. Soc.* **2011**, *137*, 934–947. [CrossRef]
23. Vincent, C.L.; Lane, T.P. Evolution of the diurnal precipitation cycle with the passage of a Madden–Julian oscillation event through the Maritime Continent. *Mon. Weather Rev.* **2016**, *144*, 1983–2005. [CrossRef]
24. Yokoi, S.; Mori, S.; Katsumata, M.; Geng, B.; Yasunaga, K.; Syamsudin, F.; Nurhayati; Yoneyama, K. Diurnal cycle of precipitation observed in the western coastal area of Sumatra Island: Offshore preconditioning by gravity waves. *Mon. Weather Rev.* **2017**, *145*, 3745–3761. [CrossRef]
25. Yokoi, S.; Mori, S.; Syamsudin, F.; Haryoko, U.; Geng, B. Environmental conditions for nighttime offshore migration of precipitation area as revealed by in situ observation off Sumatra Island. *Mon. Weather Rev.* **2019**, *147*, 3391–3407. [CrossRef]
26. Zhou, L.; Wang, Y. Tropical Rainfall Measuring Mission observation and regional model study of precipitation diurnal cycle in the New Guinean region. *J. Geophys. Res. Atmos.* **2006**, *111*, D17104. [CrossRef]
27. Fujita, M.; Kimura, F.; Yoshizaki, M. Morning precipitation peak over the Strait of Malacca under a calm condition. *Mon. Weather Rev.* **2010**, *138*, 1474–1486. [CrossRef]
28. Dipankar, A.; Webster, S.; Huang, X.-Y. Understanding biases in simulating the diurnal cycle of convection over the western coast of Sumatra: Comparison with pre-YMC observation campaign. *Mon. Weather Rev.* **2019**, *147*, 1615–1631. [CrossRef]
29. Short, E.; Vincent, C.L.; Lane, T.P. Diurnal cycle of surface winds in the Maritime Continent observed through satellite scatterometry. *Mon. Weather Rev.* **2019**, *147*, 2023–2044. [CrossRef]
30. Wu, P.; Hara, M.; Hamada, J.-i.; Yamanaka, M.D.; Kimura, F. Why a large amount of rain falls over the sea in the vicinity of western Sumatra Island during nighttime. *J. Appl. Meteorol. Climatol.* **2009**, *48*, 1345–1361. [CrossRef]
31. Hassim, M.; Lane, T.; Grabowski, W. The diurnal cycle of rainfall over New Guinea in convection-permitting WRF simulations. *Atmos. Chem. Phys.* **2016**, *16*, 161–175. [CrossRef]
32. Yulihastin, E.; Wahyu Hadi, T.; Sari Ningsih, N.; Ridho Syahputra, M. Early morning peaks in the diurnal cycle of precipitation over the northern coast of West Java and possible influencing factors. *Ann. Geophys.* **2020**, *38*, 231–242. [CrossRef]
33. Johnson, R.H.; Rickenbach, T.M.; Rutledge, S.A.; Ciesielski, P.E.; Schubert, W.H. Trimodal characteristics of tropical convection. *J. Clim.* **1999**, *12*, 2397–2418. [CrossRef]
34. Tian, B.; Waliser, D.E.; Fetzer, E.J. Modulation of the diurnal cycle of tropical deep convective clouds by the MJO. *Geophys. Res. Lett.* **2006**, *33*, L20704. [CrossRef]
35. Ichikawa, H.; Yasunari, T. Propagating diurnal disturbances embedded in the Madden-Julian Oscillation. *Geophys. Res. Lett.* **2007**, *34*, L18811. [CrossRef]
36. Vincent, C.L.; Lane, T.P. A 10-year austral summer climatology of observed and modeled intraseasonal, mesoscale, and diurnal variations over the Maritime Continent. *J. Clim.* **2017**, *30*, 3807–3828. [CrossRef]
37. Seiki, A.; Yokoi, S.; Katsumata, M. The impact of diurnal precipitation over Sumatra Island, Indonesia, on synoptic disturbances and its relation to the Madden-Julian Oscillation. *J. Meteorol. Soc. Jpn. Ser. II* **2021**, *99*, 113–137. [CrossRef]
38. Lubis, S.W.; Jacobi, C. The modulating influence of convectively coupled equatorial waves (CCEWs) on the variability of tropical precipitation. *Int. J. Climatol.* **2015**, *35*, 1465–1483. [CrossRef]
39. Sakaeda, N.; Kiladis, G.; Dias, J. The diurnal cycle of rainfall and the convectively coupled equatorial waves over the Maritime Continent. *J. Clim.* **2020**, *33*, 3307–3331. [CrossRef]
40. Ferrett, S.; Yang, G.Y.; Woolnough, S.J.; Methven, J.; Hodges, K.; Holloway, C.E. Linking extreme precipitation in Southeast Asia to equatorial waves. *Q. J. R. Meteorol. Soc.* **2020**, *146*, 665–684. [CrossRef]

41. Peatman, S.C.; Schwendike, J.; Birch, C.E.; Marsham, J.H.; Matthews, A.J.; Yang, G.-Y. A Local-to-Large Scale View of Maritime Continent Rainfall: Control by ENSO, MJO, and Equatorial Waves. *J. Clim.* **2021**, *34*, 8933–8953. [CrossRef]
42. Lubis, S.W.; Respati, M.R. Impacts of convectively coupled equatorial waves on rainfall extremes in Java, Indonesia. *Int. J. Climatol.* **2021**, *41*, 2418–2440. [CrossRef]
43. Peatman, S.C.; Matthews, A.J.; Stevens, D.P. Propagation of the Madden–Julian Oscillation through the Maritime Continent and scale interaction with the diurnal cycle of precipitation. *Q. J. R. Meteorol. Soc.* **2014**, *140*, 814–825. [CrossRef]
44. Birch, C.; Webster, S.; Peatman, S.; Parker, D.; Matthews, A.; Li, Y.; Hassim, M. Scale interactions between the MJO and the western Maritime Continent. *J. Clim.* **2016**, *29*, 2471–2492. [CrossRef]
45. Rauniyar, S.P.; Walsh, K.J. Scale interaction of the diurnal cycle of rainfall over the Maritime Continent and Australia: Influence of the MJO. *J. Clim.* **2011**, *24*, 325–348. [CrossRef]
46. Fujita, M.; Yoneyama, K.; Mori, S.; Nasuno, T.; Satoh, M. Diurnal convection peaks over the eastern Indian Ocean off Sumatra during different MJO phases. *J. Meteorol. Soc. Jpn. Ser. II* **2011**, *89*, 317–330. [CrossRef]
47. Kamimera, H.; Mori, S.; Yamanaka, M.D.; Syamsudin, F. Modulation of diurnal rainfall cycle by the Madden-Julian Oscillation based on one-year continuous observations with a meteorological radar in west Sumatera. *SOLA* **2012**, *8*, 111–114. [CrossRef]
48. Harjupa, W.; Shimomai, T.; Hashiguchi, H.; Fujiyoshi, Y.; Kawashima, M. Differences in Mechanisms of Orographic Rainfall over West Sumatra (Case Study: 10 April and 23 April 2004). *Jurnal Ilmu Fisika | Universitas Andalas* **2021**, *13*, 8–17. [CrossRef]
49. Xavier, P.; Rahmat, R.; Cheong, W.K.; Wallace, E. Influence of Madden-Julian Oscillation on Southeast Asia rainfall extremes: Observations and predictability. *Geophys. Res. Lett.* **2014**, *41*, 4406–4412. [CrossRef]
50. Muhammad, F.R.; Lubis, S.W.; Setiawan, S. Impacts of the Madden–Julian oscillation on precipitation extremes in Indonesia. *Int. J. Climatol.* **2021**, *41*, 1970–1984. [CrossRef]
51. Zhu, B.; Pu, Z.; Putra, A.W.; Gao, Z. Assimilating C-Band Radar Data for High-Resolution Simulations of Precipitation: Case Studies over Western Sumatra. *Remote Sens.* **2022**, *14*, 42. [CrossRef]
52. Huffman, G.J.; Bolvin, D.T.; Braithwaite, D.; Hsu, K.; Joyce, R.; Xie, P.; Yoo, S.-H. NASA global precipitation measurement (GPM) integrated multi-satellite retrievals for GPM (IMERG). *Algorithm Theor. Basis Doc. (ATBD) Version* **2015**, *4*, 26.
53. Tan, J.; Huffman, G.J.; Bolvin, D.T.; Nelkin, E.J. IMERG V06: Changes to the morphing algorithm. *J. Atmos. Ocean. Technol.* **2019**, *36*, 2471–2482. [CrossRef]
54. Hersbach, H.; Bell, B.; Berrisford, P.; Hirahara, S.; Horányi, A.; Muñoz-Sabater, J.; Nicolas, J.; Peubey, C.; Radu, R.; Schepers, D. The ERA5 global reanalysis. *Q. J. R. Meteorol. Soc.* **2020**, *146*, 1999–2049. [CrossRef]
55. Wheeler, M.C.; Hendon, H.H. An all-season real-time multivariate MJO index: Development of an index for monitoring and prediction. *Mon. Weather Rev.* **2004**, *132*, 1917–1932. [CrossRef]
56. Chen, S.S.; Houze, R.A., Jr. Diurnal variation and life-cycle of deep convective systems over the tropical Pacific warm pool. *Q. J. R. Meteorol. Soc.* **1997**, *123*, 357–388. [CrossRef]
57. Sui, C.; Lau, K.; Takayabu, Y.; Short, D. Diurnal variations in tropical oceanic cumulus convection during TOGA COARE. *J. Atmos. Sci.* **1997**, *54*, 639–655. [CrossRef]
58. Oh, J.-H.; Kim, K.-Y.; Lim, G.-H. Impact of MJO on the diurnal cycle of rainfall over the western Maritime Continent in the austral summer. *Clim. Dyn.* **2012**, *38*, 1167–1180. [CrossRef]
59. Sakaeda, N.; Kiladis, G.; Dias, J. The diurnal cycle of tropical cloudiness and rainfall associated with the Madden–Julian oscillation. *J. Clim.* **2017**, *30*, 3999–4020. [CrossRef]
60. Sakaeda, N.; Powell, S.W.; Dias, J.; Kiladis, G.N. The diurnal variability of precipitating cloud populations during DYNAMO. *J. Atmos. Sci.* **2018**, *75*, 1307–1326. [CrossRef]
61. Wapler, K.; Lane, T.P. A case of offshore convective initiation by interacting land breezes near Darwin, Australia. *Meteorol. Atmos. Phys.* **2012**, *115*, 123–137. [CrossRef]
62. Mapes, B.E.; Warner, T.T.; Xu, M. Diurnal patterns of rainfall in northwestern South America. Part III: Diurnal gravity waves and nocturnal convection offshore. *Mon. Weather Rev.* **2003**, *131*, 830–844. [CrossRef]
63. Du, Y.; Rotunno, R. Thermally driven diurnally periodic wind signals off the east coast of China. *J. Atmos. Sci.* **2015**, *72*, 2806–2821. [CrossRef]
64. Du, Y.; Rotunno, R. Diurnal cycle of rainfall and winds near the south coast of China. *J. Atmos. Sci.* **2018**, *75*, 2065–2082. [CrossRef]
65. Bai, H.; Deranadyan, G.; Schumacher, C.; Funk, A.; Epifanio, C.; Ali, A.; Endarwin; Radjab, F.; Adriyanto, R.; Nurhayati, N. Formation of Nocturnal Offshore Rainfall near the West Coast of Sumatra: Land Breeze or Gravity Wave? *Mon. Weather Rev.* **2021**, *149*, 715–731. [CrossRef]
66. Ruppert, J.H.; Zhang, F. Diurnal forcing and phase locking of gravity waves in the Maritime Continent. *J. Atmos. Sci.* **2019**, *76*, 2815–2835. [CrossRef]
67. Du, Y.; Rotunno, R.; Zhang, F. Impact of Vertical Wind Shear on Gravity Wave Propagation in the Land–Sea-Breeze Circulation at the Equator. *J. Atmos. Sci.* **2019**, *76*, 3247–3265. [CrossRef]
68. Du, Y.; Zhang, F. Banded convective activity associated with mesoscale gravity waves over southern China. *J. Geophys. Res. Atmos.* **2019**, *124*, 1912–1930. [CrossRef]
69. Du, Y.; Zhang, F.; Sun, Y.Q.; Wei, J.; Li, X. Practical and Intrinsic Predictability of Wave-Convection Coupled Bands Over Southern China. *J. Geophys. Res. Atmos.* **2021**, *126*, e2021JD034882. [CrossRef]